Engineering Geology 325 (2023) 107304

Contents lists available at ScienceDirect

Engineering Geology

journal homepage: www.elsevier.com/locate/enggeo

Coupling grid nanoindentation and surface chemical analysis to infer the mechanical properties of shale mineral phases

Jianting Du [a,*], Andrew J. Whittle [b], Liming Hu [c], Thibaut Divoux [d,e], Jay N. Meegoda [c,f]

[a] State Key Laboratory of Internet of Things for Smart City and Department of Civil and Environmental Engineering, University of Macau, Macau, China
[b] Department of Civil and Environmental Engineering, Massachusetts Institute of Technology, Cambridge, MA 02139, USA
[c] State Key Laboratory of Hydro-Science and Engineering, Tsinghua University, Beijing 100084, China
[d] MultiScale Material Science for Energy and Environment, UMI 3466, CNRS-MIT, Cambridge, MA 02139, USA
[e] ENSL, CNRS, Laboratoire de Physique, F-69342 Lyon, France
[f] Department of Civil and Environmental Engineering, New Jersey Institute of Technology, NJ 07102, USA

ARTICLE INFO

Keywords:
Shale
Grid nanoindentation
In-situ mineral identification
Mechanical properties of the constituent phases
Multi-scale mechanical model

ABSTRACT

Shale is a low-permeability, multi-phase, and multi-scale composite material with intrinsic heterogeneity in micro-texture and mineralogical composition. In this paper, relationships between the microscale texture and constituent phases of shale were investigated using SEM (scanning electron microscopy)/BSE (backscatter electron imaging)-EDS (energy-dispersive x-ray spectroscopy) methods, together with grid nanoindentation experiments. The mechanical properties of the constituent phases of the carbonate-rich Longmaxi shale samples were extracted based on the spatial distribution of mineral phases and the indentation interaction volume. We analyze the effects of particle size on the interpreted mechanical properties and establish a characteristic length scale based on a probabilistic analysis. The identified characteristic length for extracting the mechanical properties of constituent mineral phases from the grid nanoindentation technique is about 5.8–11.7 μm, i.e., up to 10 times greater than that proposed in prior research. A multi-scale mechanical model was established with considerations of a self-consistent scheme for granular morphology to link the microscopic characteristics with the multi-scale mechanical properties of shales. The modeling results show that the stiffness and the strength of the homogenized nano-porous illite/quartz aggregates in Longmaxi shale can be assessed from the nano-scale mechanical properties of the mineral phases and the nano-scale porosity. This study paves the way to accessing the mechanical properties of the constituent phases of composite materials based on the properties of their building blocks and provides extensive insights into their complex mechanical behavior, representing a major step towards developing reliable multi-scale models for engineering applications.

1. Introduction

Shales are fine-grained sedimentary rocks mainly composed of highly consolidated aggregates of clay minerals (phyllosilicates), silt-sized particles of other common soil minerals (e.g., tectosilicates such as quartz and feldspar, and carbonates), and organic matter. Shale formations play important roles in applications such as the geological containment of radioactive waste (Neuzil, 2013), extraction of natural gas (Du et al., 2018), and sequestration of carbon dioxide (Boosari et al., 2015; Elliot and Celia, 2012; Middleton et al., 2014). The engineering challenges associated with these applications require an in-depth evaluation of the mechanical and mineralogical properties of shales.

Shale is a porous, multi-phase, and multi-scale composite material with intrinsic heterogeneity in microtexture, mineralogy, and mechanical properties, and hence, the accurate measurement of its bulk mechanical properties or interpretation from its constituent phases continues to be a formidable challenge for the geomechanics community. The development of nanoindentation methods, first proposed by Oliver and Pharr (1992, 2004), makes it possible to obtain the local mechanical properties of composite material at micro- and nano-scales. In that framework, the grid-indentation approach can probe constituents' mechanical properties in highly heterogeneous and multi-phase materials, such as shales and concretes (Bobko and Ulm, 2008; Constantinides et al., 2006; Ulm and Abousleiman, 2006; Ulm et al., 2007). Furthermore, statistical deconvolution through a multivariate Gaussian Mixture Model (GMM) can be applied to identify the local mechanical

* Corresponding author.
E-mail address: jiantingdu@um.edu.mo (J. Du).

https://doi.org/10.1016/j.enggeo.2023.107304
Received 19 March 2023; Received in revised form 14 July 2023; Accepted 7 September 2023
Available online 12 September 2023

properties of individual constituent phases (Liu et al., 2018; Liu et al., 2021; Luo et al., 2021; Luo et al., 2020; Wu et al., 2020; Xu et al., 2020). However, this prior work has applied statistical analyses of the mechanical data without direct reference to the local mineralogy and hence, phases of different mineralogy but similar mechanical response, as well as their mixtures, may manifest as a single microstructural component potentially resulting in bias of the statistical deconvolution analysis. Although further efforts have been made to reflect the mineralogy by using electron probe microanalyzer (EPMA) techniques (Abedi et al., 2016; Deirieh et al., 2012; Mashhadian et al., 2018; Veytskin et al., 2017), the direct link between the nanoindentation measurements and local mineralogy to infer mechanical properties of shale mineral phases has not been established to date.

Recently, Liu et al. (2022) studied the nano-scale mechanical properties of constituent minerals in shales by combining nanoindentation statistical analyses and SEM-EDS-XRD techniques. The residual impressions of nanoindentation grids were visually checked under SEM/BSE imaging and the local mineralogy under the residual impressions was analyzed using EDS measurements. In this case, the measurements should correspond to mineral phases within the deformed zone, rather than those directly under the indent impression. This is illustrated by considering the stress conditions beneath an indenter (Fig. 1a). Elasto-plastic deformations can occur within a highly stressed zone beneath the indenter tip contact that is 10 times greater than the indentation depth (Durst et al., 2005; Woodcock and Bahr, 2000). Moreover, particle size effects and similarities in the mechanical properties of certain mineral phases can result in bias in evaluating nano-scale mechanical properties.

In a shale sample, with a broad range of particle sizes, the process zone can either be contained within a single mineral phase or be influenced by particles of distinct constituent phases (and hence, represent local homogenization of the individual phases), as illustrated in Fig. 1b. Moreover, the volume fractions of the constituent phases are closely linked to the bulk mechanical properties of shale (Abedi et al., 2016; Kuila et al., 2014). However, the prior studies generally infer volume fractions of minerals from mass fractions using semi-quantitative XRD methods (with average densities reported independently) (Abedi et al., 2016; Chen et al., 2015).

In light of these limitations, we have investigated the nano-scale properties of individual shale phases by combining grid nanoindentation data with high-resolution digital mineralogy maps. The particle size distributions of constituent mineral phases are extracted with an edge detection algorithm to better estimate nano-scale mechanical properties. We show how these nano-scale properties of individual shale phases can be reliably determined and upscaled to estimate the macro-scale homogeneous mechanical properties of the composite material.

2. Materials and methods

2.1. Samples and surface preparation

The samples used in this research are from the Silurian Longmaxi Formation in Sichuan Basin, China. This shale is composed of abundant brittle minerals, mainly feldspar, mica, quartz, and carbonate (average 56.3%) and displays a relatively high porosity ranging from 1.2 to 10.8% (Dai et al., 2014). The shale samples do not show any visible bedding planes. Small cuboidal specimens with dimensions (2 cm × 2 cm × 1 cm; Length × Width × Thickness) were trimmed from large shale block samples using an IsoMet 1000 precision saw (Buehler Inc., IL, USA). A total of seven trimmed shale specimens (M1 - M7) were used to enable comparisons across specimens from different locations and target test patches.

Two surface preparation methods were investigated in this study. The first method consists of dry-mechanical polishing (using SiC paper with grit size >0.25 mm) and ultrasonication in n-decane solution; while the second involves Argon milling using a cross-section polisher (JEOL Inc., MA, USA) with a maximum accelerating voltage of 6 kV (to minimize heat damage). Appendix A summarizes the specification of the procedures of Argon milling.

The surface roughness of the polished specimens was measured using an Atomic Force Microscope (AFM) (Oxford Instruments Asylum Research Inc., CA, USA) with a wave mode or 'tapping' scan (Simpson et al., 1999). The specimens were characterized by a roughness $R_q = 15$ nm and 50 nm for mechanical polishing and Argon milling, respectively. Following prior studies (Bobji and Biswas, 1999; Donnelly et al., 2006), which involve indentation depth h such that $h > 3R_q$, experiments in this study were designed with a target penetration depth of 100 nm to 400 nm. Fig. A2 shows that the polishing method had minimal impact on the engineering properties computed from grid indentation experiments; hence, the data reported in this paper are all based on specimens prepared by the more efficient mechanical polishing method.

2.2. Grid nanoindentation tests

Indentation measurements were performed on seven mechanically-polished specimens (M1 - M7) of carbonate-rich Longmaxi shale using a NanoTest indenter (Anton Paar, Graz, Austria) equipped with a Berkovich tip (half-angle 70.32° and curvature radius of approximately 30 nm). The setup allows applying loads ranging between 0.1 and 500 mN with a resolution of 0.04 μN. Indentation tests were performed on a square grid ($n^2 = 21 \times 21$) with 10 μm separation (total patch area, $A = 0.04$ mm^2) to avoid interactions between adjacent indents (Ulm and Abousleiman, 2006). Each test followed a standard loading function to a prescribed maximum force of 4.0 mN, resulting in a maximum indentation depth varying between 100 nm and 400 nm according to the local mineralogy and particle texture. The load was held constant for 2 mins before unloading (with $|dF/dt| = 15$ mN/min in both loading and unloading). From each indentation test, two quantities were computed. First, the hardness, H, is defined as follows:

$$H = \frac{F_{max}}{A_c} \tag{1}$$

where F_{max} is the maximum indentation load, and A_c is the projected contact area. The contact area function is well-defined for a perfectly sharp Berkovich tip. In practice, however, the Berkovich indenter exhibits some bluntness, which can significantly affect the interpretation of results, especially for shallow indentations. Thus, in this study, A_c is determined by indentation on a material whose mechanical properties are known (e.g., fused silica, which has an indentation modulus $M = 72$ GPa). A_c is a function of the contact depth, h_c:

$$A_c = C_1 h_c^2 + C_2 h_c + C_3 h_c^{1/2} + C_4 h_c^{1/4} + \ldots \tag{2}$$

$$h_c/h_{max} = 1 - \varepsilon F_{max}/(S h_{max}) \tag{3}$$

where C_1 is usually determined by the area-to-depth constant of the perfectly sharp indenter (e.g., for a Berkovich indenter, $C_1 = 24.58$) and $\{C_i\}_{i>1}$ are the factors that attribute to the bluntness of the indenter. ε is a constant related to the geometry of the indenter, and S is the contact stiffness, which can be calculated by evaluating the derivative at the maximum load:

$$S = \left.\frac{\delta F}{\delta h}\right|_{h_{max}} \tag{4}$$

The Young's modulus, E, of the indented bulk material can then be obtained from the unload force-displacement curve:

$$E = \left(1 - \nu^2\right) \Big/ \left(\frac{1}{M} - \frac{1 - \nu_i^2}{E_i}\right) \tag{5}$$

where ν and ν_i are the Poisson's ratio of the test sample and the diamond indenter (0.07), respectively; M is the reduced or indentation modulus,

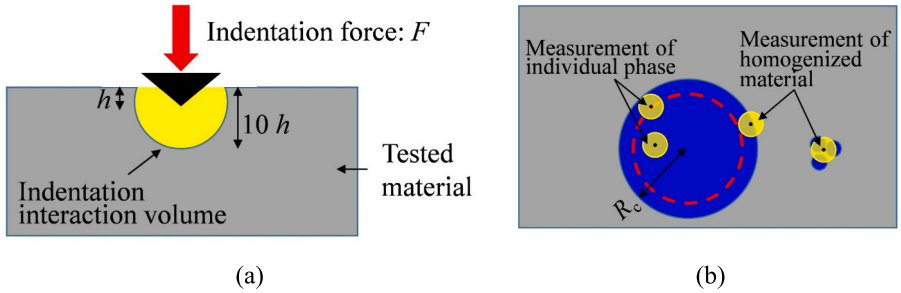

Fig. 1. Effects of particle size on indentation measurements. a) Influence zone deformed in an elastoplastic fashion beneath the indenter tip; b) Particles (blue) with characteristic dimension R_c embedded in a matrix (gray). Indents at the edge of large particles or impinging on small inclusions will measure the homogenized response of the two phases. (For interpretation of the references to colour in this figure legend, the reader is referred to the web version of this article.)

which coincides with the plane stress modulus for rigid indentation of an isotropic material; E_i is Young's Modulus of the diamond indenter (1140 GPa).

Poisson's ratio of shales has been measured and reported in the literature. Typical ranges $\nu = 0.1–0.3$ and 0.15–0.35 have been reported in prior studies for Longmaxi shale (Chen et al., 2018; Yang et al., 2016) and Barnett shale (Guo et al., 2013), respectively. Here, we assume $\nu = 0.2$ for interpreting E across all samples. Prior work has demonstrated that the uncertainty on ν has limited influence on the estimation of E (Oliver and Pharr, 1992; Zhang et al., 2009).

2.3. Method to interpret local mineralogy

The test procedure, illustrated in Fig. 2, involves the selection of the area tested by grid nanoindentation using SEM imaging, followed by the insertion of electron backscatter diffraction (EBSD) analyzers to generate the BSE image and EDS map with a resolution of 800 × 1024 pixels (0.24 mm × 0.3 mm), each pixel corresponding to 300 nm × 300 nm. The quantitative element information stored in each pixel was then extracted through a Matlab code. The unique elements of each mineral phase are used for mineralogical identification. For instance, co-existence of silicon, aluminum and potassium in a pixel is used to identify illite, while silicon alone (i.e., no magnesium, iron, sulfur, aluminum, and potassium are detected in the pixel) is used to identify as the quartz phase. Carbon and oxygen are not used as unique elements to analyze the mineral phases due to their wide existence in most of the constituent phases in shale. Based on the elemental chemical composition in each pixel, the in-situ mineralogy can be uniquely identified pixel by pixel. Finally, a 'digital mineralogy map' was obtained that determines the edges of particles, the area fraction, and the spatial distribution of each component phase. The results of this approach are illustrated in Fig. 3. They closely match the microstructure observed in the BSE image of the same region, with six pure mineral phases (illite, quartz, calcite, dolomite, pyrite, and organics) and up to six mixed phases.

2.4. Matching of mineralogy and indenter footprint

In order to assign the nano-scale mechanical properties inferred from the nanoindentation grid to their corresponding mineral phases, it is

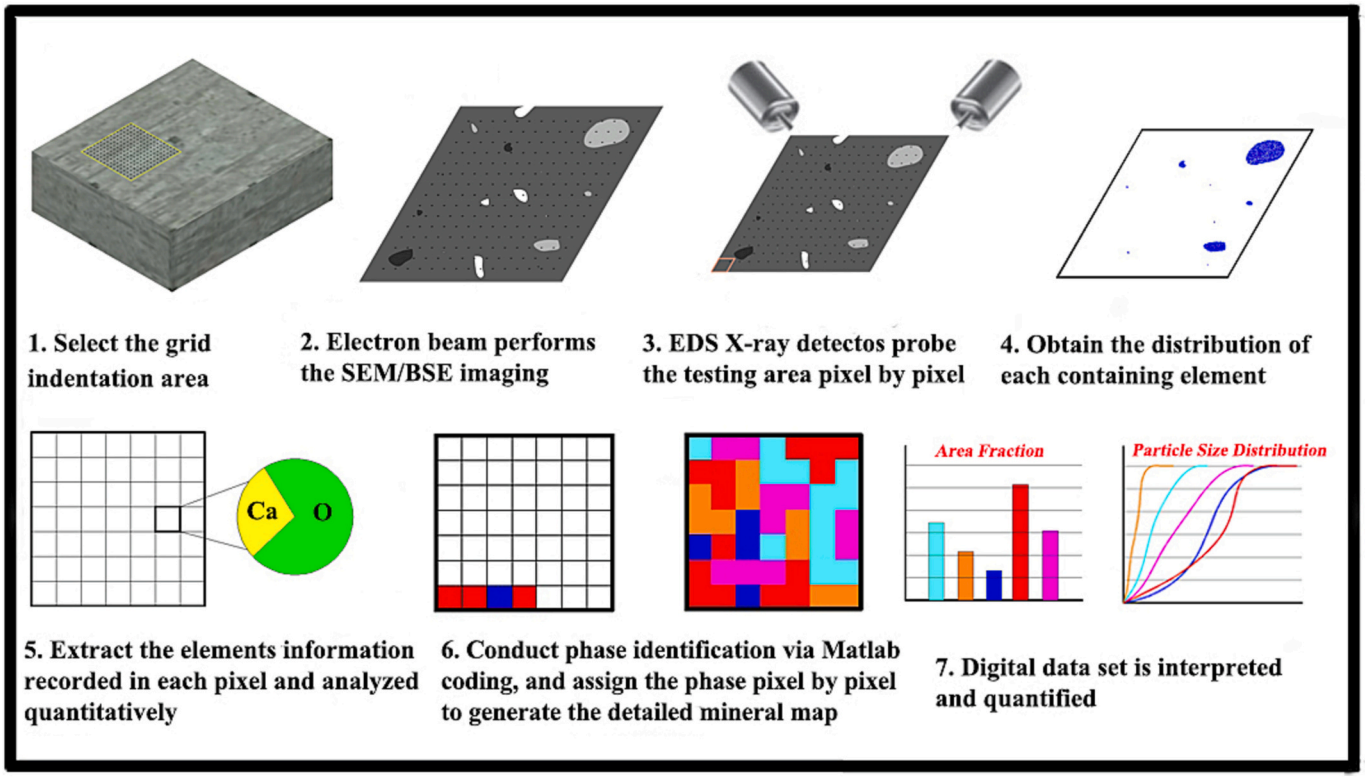

Fig. 2. Procedure for in-situ mineralogical identification.

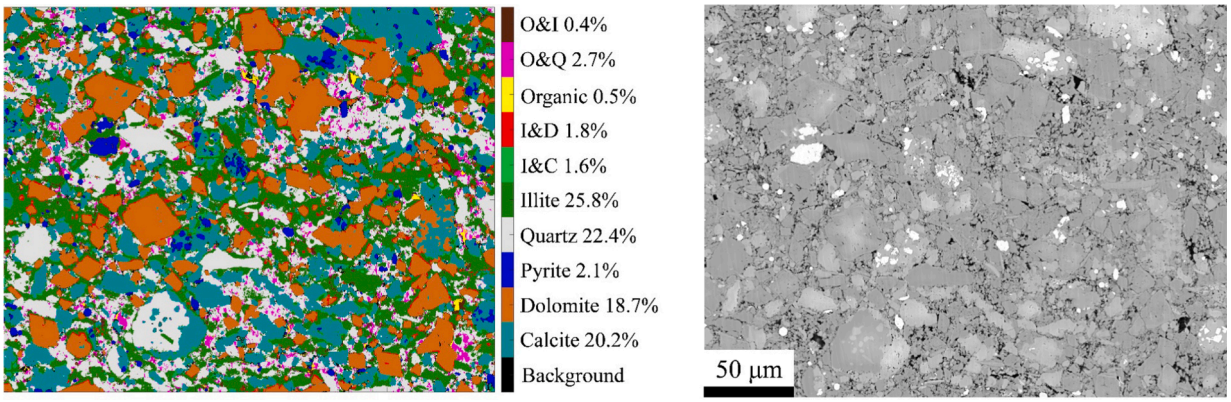

Fig. 3. a) 'Digital mineralogy map' generated by the in-situ mineralogical identification technique and b) BSE image of the same region of interest (ROI). The labels 'C', 'D', 'Q', 'I', and 'O' represent calcite, dolomite, quartz, illite, and organic, respectively. The particles of mineral phases, which appear with different gray scales in the BSE image, agree with the identification results in the 'digital mineralogy map'.

essential to obtain precisely the spatial information of the nanoindentation grid. However, due to the size of each indentation footprint and the lack of contrast between the footprint and the tested shale surface, it is impossible to distinguish individual indents while visualizing the entire nanoindentation grid in the region of interest. Thus, in this study, BSE scanning was used to locate the four corners of the grid (from the indentation footprints) and adjacent key morphological features, as illustrated in Fig. 4a. Then, the individual indents were determined assuming a regular pattern for the nanoindentation grid (rows and columns are perpendicular with each other), as illustrated in Fig. 4b.

The projected area of each indent was calculated according to the measured penetration depth [Eq. (2)] and superimposed on the pixel-scale digital mineralogy map (Fig. 5). The constituent mineral phases were assigned to the pixels included in the indentation interaction volume based on the spatial information of the mineral phases in the in-situ 'digital mineralogy map' and the coordinates of the indentation grid. The related mineral phase was then classified either as a single constituent phase (> 90% of the pixels display the same mineralogy) or a mixed phase based on the pixel ratio, which defines the number of pixels displaying the same mineralogy in the indentation interaction volume, N_m, to the total number of the pixels included in the interaction volume, N_t, i.e., N_m/N_t. We adopt a conservative rule of thumb, if the proportion of other minor identified constituents is lower than 10%, the measured phase is considered a pure mineral phase (e.g., calcite phase). The measured phase is classified as a mixture phase if two or more phases, each representing >10%, are present.

2.5. Particle size distribution of mineral phases

Particle size distributions of shale mineral phases are quantified by processing the digital mineralogy map (Fig. 3). An edge detection algorithm, which has been widely used for quantitative analysis of particle and pore size in a porous medium such as soil and rock (Jiu et al., 2018; Jiu et al., 2020; Wu and Yu, 2012; Zhou et al., 2018), is applied using a customized Matlab code. Small holes inside the particles of mineral phases (see, e.g., red circles in Fig. 6) are filled first. Then the boundary

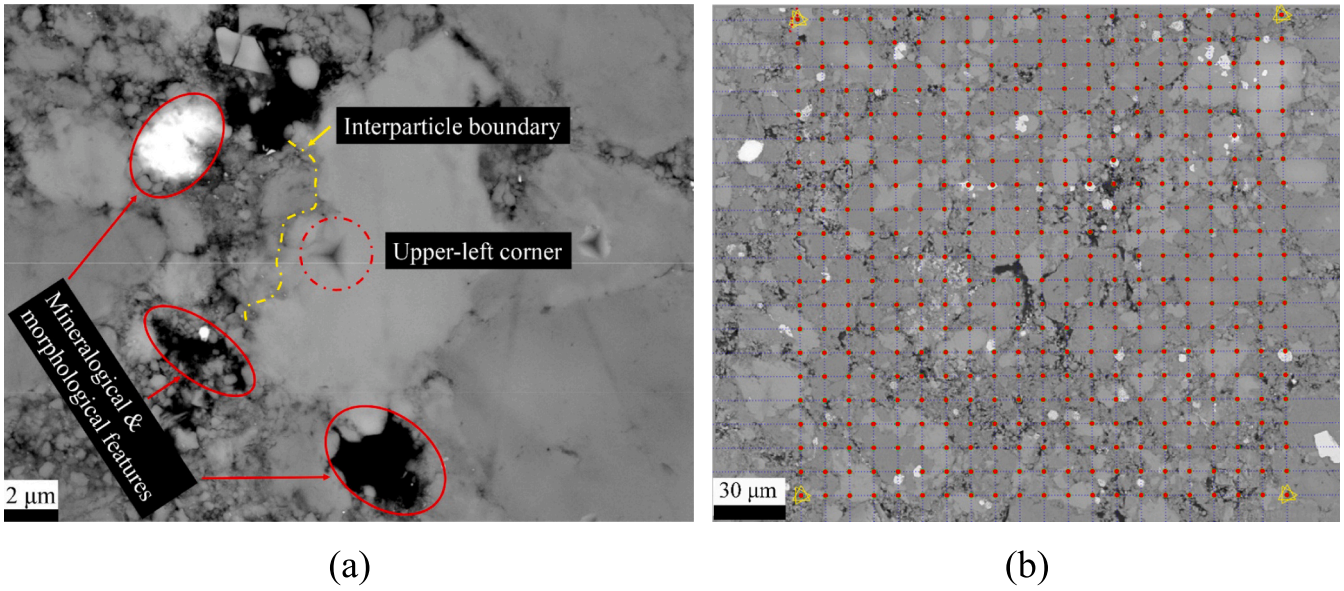

Fig. 4. Determination of nanoindentation grid coordinates. (a) Mineralogical and morphological features in the vicinity of the top-left corner point of the indentation grid observed by high-magnification BSE imaging; (b) indentation grid overlaying the BSE image of the ROI. The grid is positioned assuming a perfectly squared grid based on the knowledge of the corner coordinates.

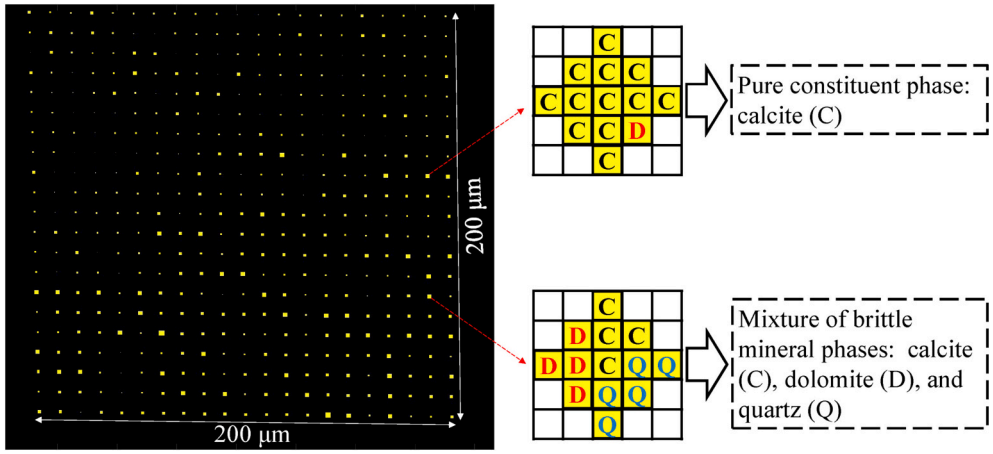

Fig. 5. Mechanical and mineralogical information matching.

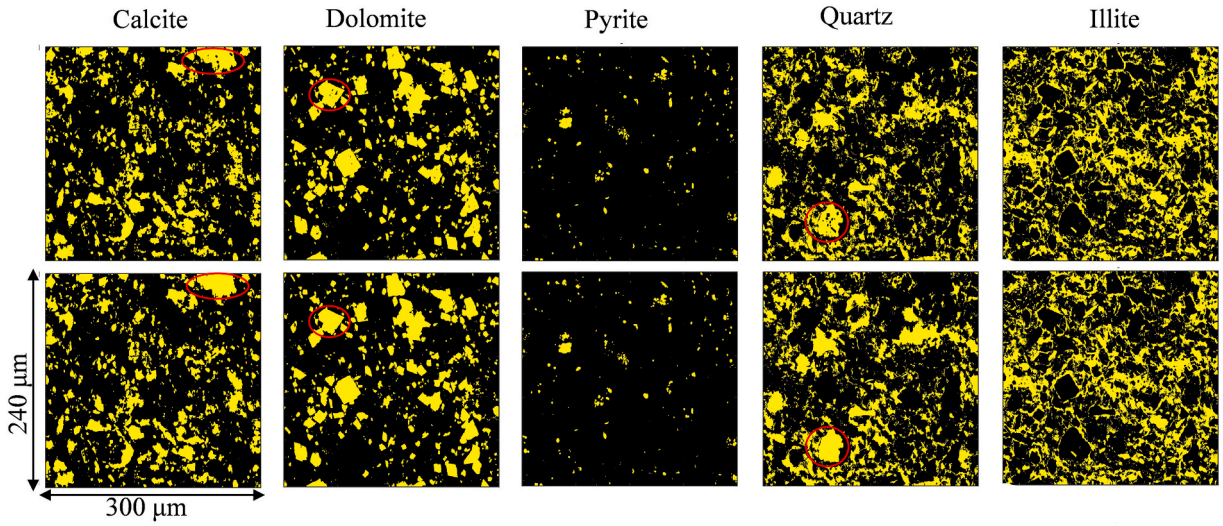

Fig. 6. Procedures for particle size calculation. The first row shows the distribution map of each mineral phase identified by the in-situ mineralogical identification. Small holes inside each isolated particle (see red circled) are filled before counting and recording the number of pixels occupied by each particle (the second row). (For interpretation of the references to colour in this figure legend, the reader is referred to the web version of this article.)

of each particle is identified by the connection algorithm, which labels connected components in 2D binary image before counting and recording the number of pixels occupied by each particle. Finally, based on the relationship between the actual length and pixel size, the true area of each particle is calculated, which allows us to compute the cumulative distribution of particle area for each mineral phase. It should be noted that particles or pores with a size smaller than the pixel size (300 nm × 300 nm) cannot be detected in this analysis.

3. Results

3.1. Mineralogy and particle size distribution

Fig. 7 shows two high-resolution digital maps of the mineralogy of Longmaxi shale samples (specimens M3 and M4). These results highlight the complex microstructure of shale, which is characterized principally by five mineral phases, i.e., quartz, calcite, dolomite, illite, and pyrite. These phases constitute about 90% of the surface area, among which pyrite and organics display much smaller fractions. Since each pixel in the digital mineralogy map corresponds to an area of 300 nm × 300 nm, up to 6 mixed phases (with a total area fraction of about 5.5%) were detected at the junctions between different mineral phases. These mixed phases were further classified into three categories: 1) brittle mixtures (any combination of calcite, C, dolomite, D, quartz, Q and pyrite, P); 2) ductile mixtures (combination of organic, O, and illite, I); and 3) composite mixtures (combinations of minerals from both brittle and ductile groups). Specifically, the C&Q and D&Q phases were classified as brittle mixtures, whereas the I&O phase was classified as a ductile mixture. Finally, the I&C, I&D, and I&Q phases are classified as composite mixtures. Table 1 summarizes the area fractions of the pure and mixed phases (found in 8 regions of interest) for the seven specimens of the carbonate-rich Longmaxi shale. The measured area fraction of each mineral phase exhibited a relatively small standard deviation (of about 0.5– 5%) over the ROI (240 μm × 300 μm).

The digital mineralogy maps also illustrate the complex microstructure of the Longmaxi shale, with a wide range of particle sizes for each mineral phase. Fig. 8 shows a representative result of the studied shale's cumulative particle area distribution functions (measured on specimen M5). This data reveals that the carbonate minerals (calcite and dolomite) were associated with larger particles than quartz, illite, and pyrite. Given that the maximum penetration depth for the grid indentation tests ranged from 100 to 400 nm; hence, the projected area of an indentation interaction volume ranged from 5 to 15 μm^2. Therefore, Fig. 8 shows that the indentation footprint can exceed up to 20% of the quartz, illite, and pyrite particles but only 5% for calcite and dolomite. The high proportion of fine particles ($\leq$ 15 μm^2) increases the

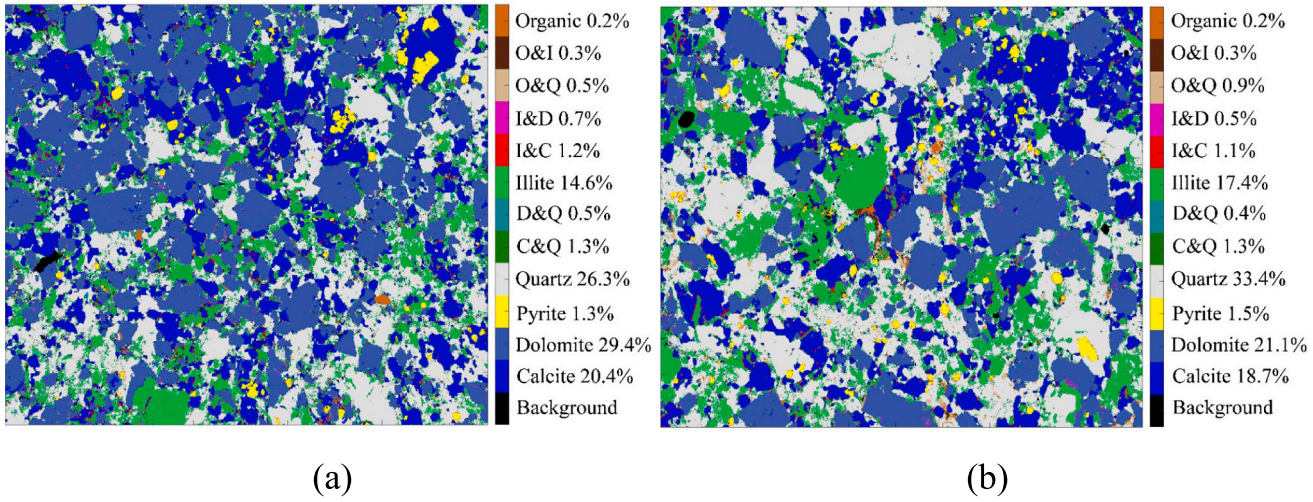

Fig. 7. Quantitative mineralogical maps (240 μm × 300 μm) for samples M3 (a) and M4 (b) obtained by in-situ mineralogical identification.

Table 1
Area fractions of mineral phases in carbonate-rich Longmaxi shale.

Sample ID	Calcite (%)	Dolomite (%)	Pyrite (%)	Quartz (%)	Illite (%)	Organic (%)	C&Q (%)	D&Q (%)	I&C (%)	I&D (%)	O&Q (%)	O&I (%)
M1	20.2	18.7	2.1	22.4	25.8	0.5	–	–	1.6	1.8	2.7	0.4
M2	17.5	14.1	1.8	36.2	21.5	0.3	0.6	–	1.7	0.8	2.0	1.2
M3	20.4	29.0	1.3	26.3	14.6	0.2	0.2	0.5	1.2	0.7	0.3	0.3
M4	18.7	21.1	1.5	33.4	17.4	0.2	1.3	0.4	1.1	0.5	0.9	0.3
M5	25.8	26.1	2.1	14.6	20.5	0.06	1.4	0.6	2.1	1.5	0.6	–
M6	23.5	24.5	1.8	19.4	22.6	0.3	0.8	–	1.2	0.7	0.2	0.5
M7	19.4	22.4	2.3	23.9	23.1	0.1	–	0.6	0.5	1.0	1.5	0.8
Mean	20.7 ± 2.7	22.3 ± 4.6	1.8 ± 0.3	25.1 ± 7.0	20.7 ± 3.4	0.2 ± 0.1	0.9 ± 0.4	0.5 ± 0.08	1.3 ± 0.5	1.0 ± 0.4	1.2 ± 0.9	0.6 ± 0.3

Note: Results were obtained from seven specimens of carbonate-rich Longmaxi shale. The labels 'C', 'D', 'Q', 'I', and 'O' represent calcite, dolomite, quartz, illite, and organic, respectively. The C&Q and D&Q phases are classified as brittle mixtures, whereas the I&O phase is classified as a ductile mixture. The I&C, I&D, and I&Q phases are classified as composite mixtures.

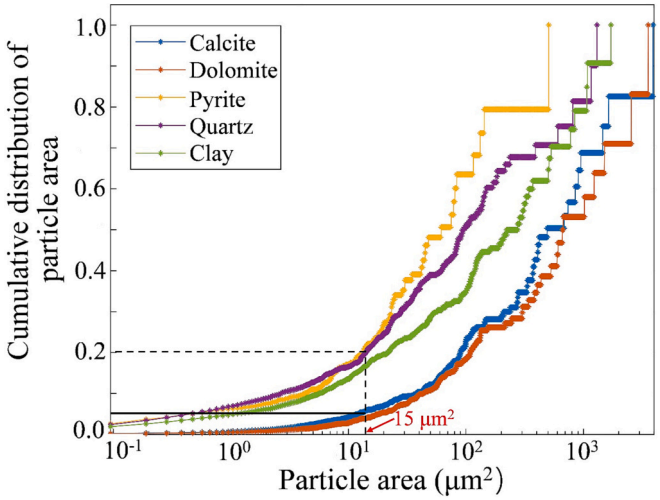

Fig. 8. Cumulative particle area distribution functions of calcite, dolomite, quartz, and pyrite phases measured in sample M5. The projected area of an indentation interaction volume can be up to 15 μm², corresponding to ~20% for quartz, pyrite, and illite phases but only ~5% for calcite and dolomite.

probability that a mixture of mineral phases will affect the indentation measurements and corresponding engineering properties. More detailed observations from the SEM/BSE images showed two distinct morphologies of quartz, illite, and pyrite minerals within the Longmaxi shale: 1) larger intact particles and 2) porous aggregates of fine grains with nano-scale interparticle pores. It should be noted that particles or pores with a size smaller than the pixel size of the digital mineralogy map (300 nm × 300 nm) cannot be detected in this analysis. Thus, the cumulative area distribution for illite includes both intact particles and nano-porous aggregates.

Fig. 9a illustrates the co-existence of these morphologies for quartz, for which there was a significant contrast in individual particle size. These observations were consistent with results reported by Dong et al. (2019) and Xu et al. (2021), who also identified different forms of quartz in the Longmaxi shale. Similarly, the Longmaxi shale specimens included isolated larger pyrite particles and framboidal structures (Fig. 9b) that have been reported for other shales (e.g., Opalinus (Seiphoori et al., 2017)). In contrast, carbonate minerals were mostly found as isolated particles.

3.2. Mechanical properties of mineral phases from grid nanoindentation

Fig. 10 shows the local mineral phases at the locus of each indentation superimposed with the BSE image. Here, nine distinct mineral phases are identified, including six pure phases (cf. Table 1 including organics), and three mixtures (i.e., brittle, ductile, and composite). Notably, although mixed phases characterize only 5.5% of the ROI surface area at the pixel scale (Fig. 7), 30–40% of the indentation footprints were classified as mixtures. This is due to the greater size of the indentation interaction volume (up to 1 μm × 1 μm) when compared to the pixel size (300 nm × 300 nm), which in turn resulted in a higher probability of measuring a mixture. Fig. 11a and b illustrate in more

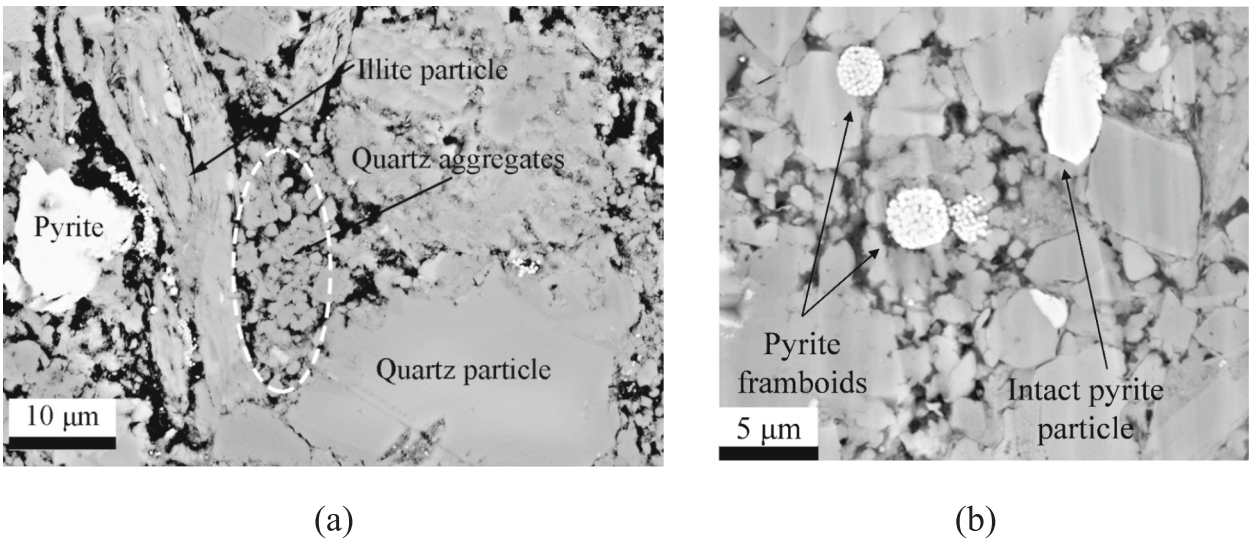

Fig. 9. Representative BSE image showing granular aggregates and isolated particles of mineral phases in shale: (a) quartz and (b) pyrite.

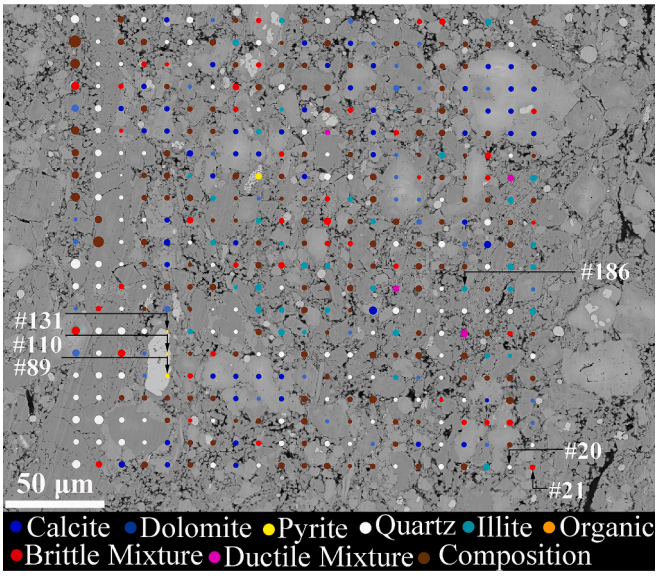

Fig. 10. Indentation-mineral map (sample M2) showing local mineral phases at the locus of each indentation superimposed with the BSE image. Indentation points are randomly selected to verify the accuracy of the measured indentation-mineral map.

detail the accuracy of the indentation-mineral map by interpreting the indentation footprints and mineralogy of the randomly selected indent locations (as shown in Fig. 10). These examples show that the proposed coupled analysis of grid-nanoindentation and in-situ mineralogical identification provides a precise and reliable toolkit for identifying nano-scale mechanical mineralogical information in a complex composite material such as shale.

All the indentation data from grid indentation experiments on specimens M3 - M7 (in total 441 × 5 = 2205 indentations) were integrated. These data provided sufficient information for statistical analyses of each phase's mechanical properties and area fractions. Area fractions of the five pure mineral phases obtained from the statistical analysis were consistent with those measured from the in-situ mineralogical identification (Table 1).

Fig. 12a, b show raincloud plots (Allen et al., 2019) of Young's modulus, E, and hardness, H, computed from grid nanoindentation on the Longmaxi shale for five pure mineral phases and three mixed phases. These figures combine boxplots of individual indents with an interpretation assuming that these properties can be described by a single lognormal distribution for each classified phase. The data was relatively sparse for the organic phase, and the properties of the organics were reported using a mean value (E = 8.2GPa and H = 0.95 GPa), which is consistent with results reported in the literature by Eliyahu et al. (2015), Li et al. (2018), and Shukla et al. (2013). In addition, the boxplot data for quartz and illite show significant skewness (particularly for H, Fig. 12b), which indicates that the structures of the mechanical data of quartz and pyrite phases are not monophasic. The skewness confirms prior observations that particle morphology (i.e., large intact particles vs. nanoporous aggregates of quartz and illite particles) affects the results. The statistical mean of Young's modulus of clay phase shown in Fig. 12b (i.e., 41.3 GPa) is greater than the results from some other prior studies (Bobko and Ulm, 2008; Liu et al., 2018). This is because the current indentation data of the clay phase include measurements of both intact clay particles and nano-porous clay aggregates. However, in prior studies, the indentation measurement mainly focused on the porous clay composite, which has a much lower modulus and hardness than those of the intact illite particles. A comparison between Young's modulus and hardness of the five main mineral phases measured in this study and those reported in prior publications are summarized in Table 2.

The data of the composite mixture phase obtained from the above coupled analysis can be compared to measurements performed at a mesoscopic scale, beyond which the mechanical response is homogeneous. Fig. 13 compares Young's modulus and hardness values of the composite mixture phase with microindentation data (penetration depths 8–10 μm) reported for the very same specimens of Longmaxi shale (Du et al., 2021). While there is a much larger scatter in properties nanoindentation determined at the nanoscale (reflecting the different phase mixtures), the two data sets show very similar mean values of the two-dimensional Gaussian distribution. This result indicates that the homogenized mechanical properties of complex composite materials such as shale can be assessed by its nano/microscale representative unit composed of both the brittle and ductile mineral phases.

3.3. *Effects of particle size on mechanical properties*

Determining the 'characteristic' lengths of the constituent mineral phases is essential for extracting their mechanical properties from the grid nanoindentation technique. By assuming the particles for each phase are spherical with a diameter, D, and that the indentation interaction volume is five times greater than the indentation depth h, Ulm

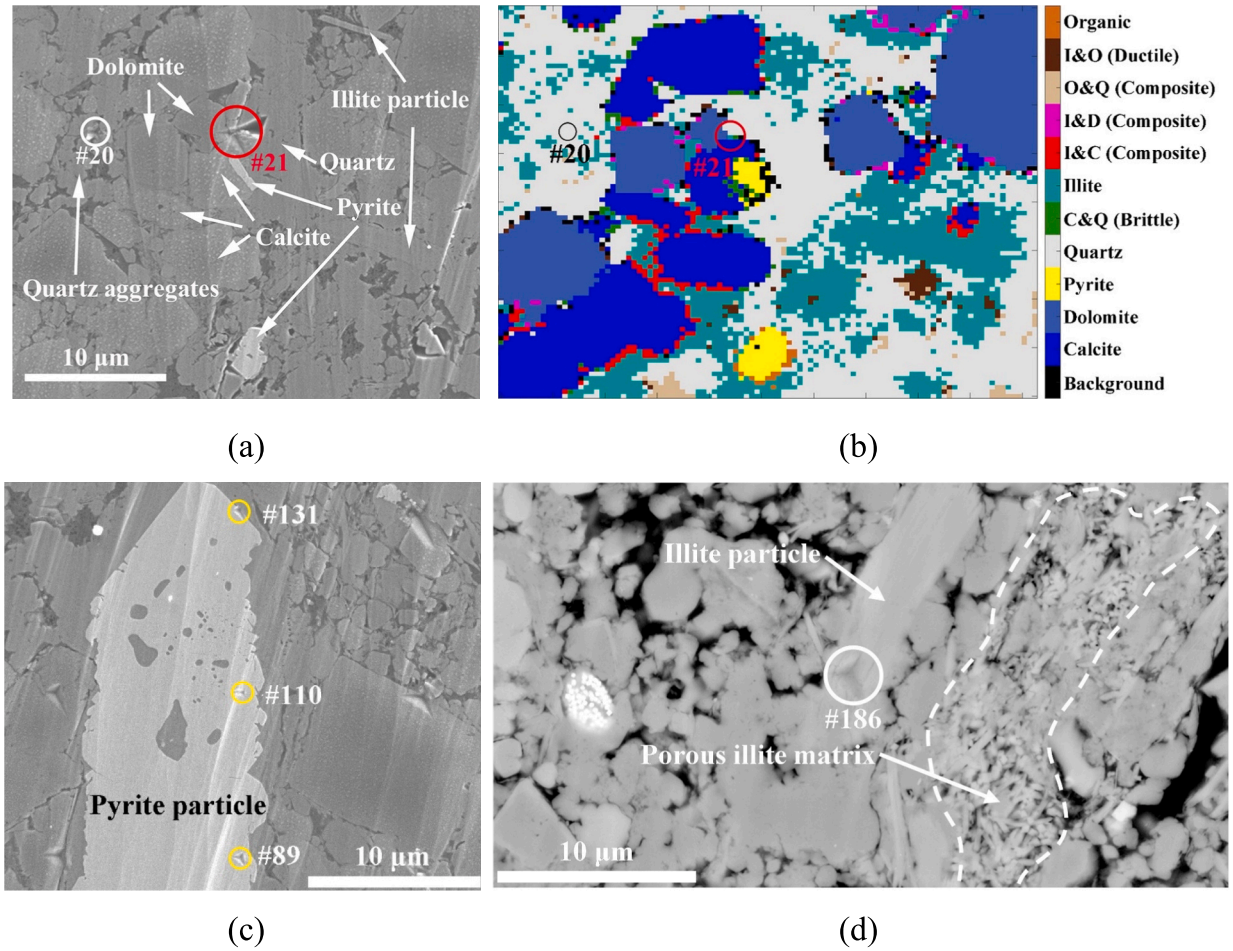

Fig. 11. Verification of the indentation-mineral map: a) Indentation footprints on a quartz phase (indent #20) and the brittle mineral mixtures (indent #21). b) Local mineralogy of indents #20 and #21. c) Indentation footprints on a single pyrite particle (indents #89, #110, #131), and d) indentation footprint on an illite particle (indent #186). These observations result from high-magnification SEM imaging and BSE imaging, respectively. The residual footprints of the selected points are circled in the SEM and BSE images.

and Abousleiman (2006) proposed that a ratio $h/D < 1/10$, will allow a reliable interpretation of mechanical properties for the constituent phases. However, this assumption does not consider indentation footprints closer to the edge of a particle, where a mixture of phases influences the mechanical response. Furthermore, the probability of indenting at the center of a spherical particle is negligible, and hence, the characteristic length is generally underestimated.

In this study, the critical characteristic lengths of the constituent mineral phases are determined based on a probabilistic analysis. Considering a nanoindentation grid randomly performed on a ROI, the mechanical properties of a given constituent mineral phase require an adequate surface area for the indentation interaction volume within a single particle. The interaction volume should be located at a minimum distance of 3 h from the particle boundary to avoid the influence of adjacent phases or pores. As a result, compared to the maximum indentation depth, the particle area should be large enough to ensure that the probability of the indentation loci within the applicable area, η, obeys the conservative rule of thumb, i.e., $\eta = 90\%$. Such a rule makes it possible to extract the mechanical properties of a specific constituent phase by statistical analysis of all the particles of that phase. Therefore, the critical characteristic length for measuring the mechanical properties of the constituent phases can be determined as follows:

$$\pi(R_c - 3h)^2 / \pi R_c^{\,2} = 0.9 \tag{6}$$

where R_c is the particle radius. In this study, maximum indentation depths range from 100 to 200 nm for the pure mineral phases (i.e., calcite, dolomite, quartz, pyrite, and illite). Therefore, the characteristic length and area of the pure mineral phases are about 5.8–11.7 μm and 100–430 μm^2, respectively, i.e., up to 10 times greater than that proposed in prior research.

The skewed distributions of mechanical properties for quartz and illite phases in Fig. 12 suggest that the pure mineral phases must be partitioned to reflect two or more particle structures. We have investigated particle size effects for quartz and illite phases based on detailed observations of their particle morphology. For example, Fig. 14a and b compare nanoindentation values of E and H for nano-porous illite aggregate with those of a much larger intact particle. The intact illite phase has a much higher modulus and hardness than those of the nano-porous phase.

The Bayesian Information Criterion (BIC) and Multidimensional Gaussian Mixture Model (GMM) (Abedi et al., 2016; Deirieh et al., 2012) were used to identify and classify morphological components for illite and quartz:

$$BIC = -2\log\widehat{L}(\theta) + nlog(N) \tag{7}$$

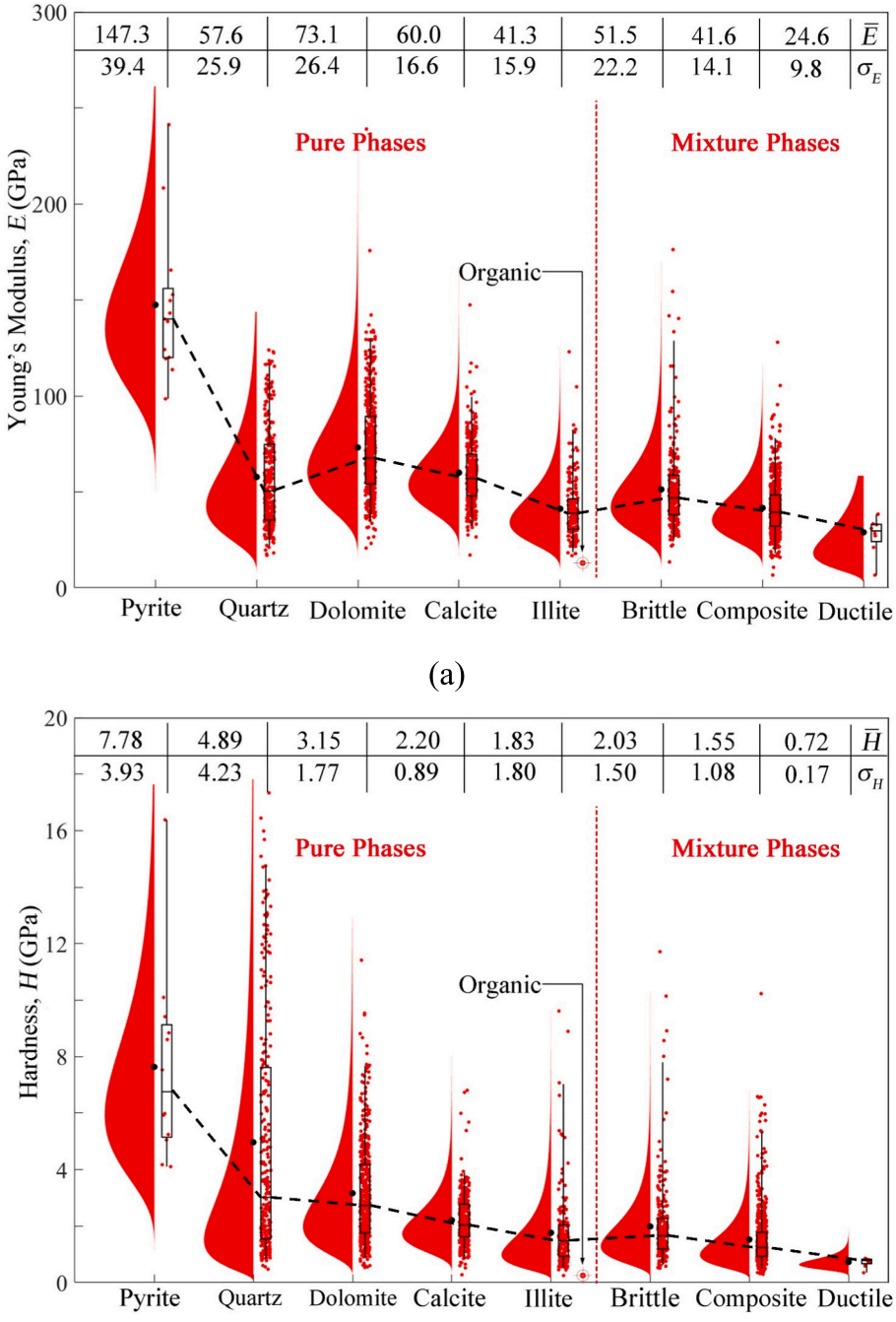

Fig. 12. Mechanical properties of the mineral phases from grid nanoindentation of M1-M7 specimens: a) Young's modulus and b) hardness. The data are presented using a raincloud format that combines conventional boxplots with median, interquartile range (IQR) box, and outlier whiskers (upper quartile +1.5 × IQR and lower quartile - 1.5 × IQR); together with interpretations assuming a single lognormal distribution function for each phase (expectation and standard deviation properties are reported in the inset in each figure). The black dots at the bottom of each distribution show the positions of the expectation ($\overline{E}$ and $\overline{H}$).

Table 2
Summary of Young's modulus and hardness of the 5 main mineral phases in Longmaxi shale samples obtained in this study and prior publications.

Mineral Phase	Coupled analysis (Fig. 12)		Refinement by BIC & GMM (Fig. 15)		Results for Intact Particles (> threshold size)		*Published Results*		
	E (GPa)	*H* (GPa)	*E* (GPa)	*H* (GPa)	*E* (GPa)	*H* (GPa)	*E* (GPa)	*H* (GPa)	*Source*
Calcite	60.0	2.20	64.3	2.4	61.2	2.3	73–83	2.1–2.4	(1)
Dolomite	57.6	3.15	85.9	4.9	93.1	4.7	53–82	3.5–7.5	(2)
Quartz	73.1	4.89	72.8	8.10	69.3	6.9	82–96	13.3–14.8	(1)
Pyrite	147.3	7.78	–	–	226.6	13.6	264–330	16–27	(3)–(6)
Illite	41.3	1.83	62.1	4.65	71.1	3.9	62	–	(7)

Note: (1) Broz et al. (2006); (2) Viktorov et al. (2014); (3) Li et al. (2022); (4) Kumar et al. (2012); (5) Aguilar-Santillan (2008); (6) Loberg et al. (1985); (7) Xian et al. (2019).

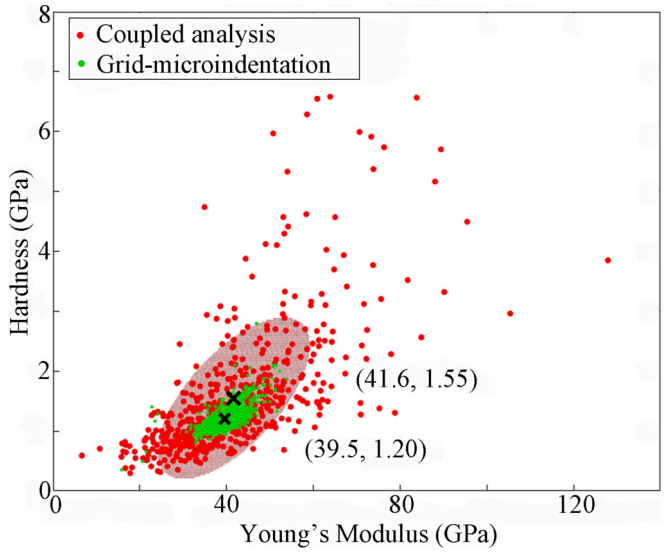

Fig. 13. Comparison between the mechanical properties (E and H) of the composite phase extracted from the coupled analysis of nanoindentation (h = 100–400 nm; red dots) and the homogenous mechanical properties measured by grid microindentation with characteristic indentation depth h = 8–10 μm (green dots) (Du et al., 2021). Values in the brackets show the statistical mean of Young's modulus and hardness expressed in GPa. The shaded ellipsoid is drawn based on the statistical confidence level of 95% and the covariance matrix, which determines the length of the major and minor axes, and the orientation of the axes, respectively. (For interpretation of the references to colour in this figure legend, the reader is referred to the web version of this article.)

$$\mathrm{j}=1,\mathrm{n};\mathrm{D}\left(\mathrm{X_i};\mu_\mathrm{j}^\mathrm{X},\mathrm{s_j^X}\right)=\frac{1}{\mathrm{s_j^X}\sqrt{2\pi}}\int_{-\infty}^{\mathrm{X_i}}exp\left(\frac{-\left(\mathrm{u}-\mu_\mathrm{j}^\mathrm{X}\right)^2}{2\left(\mathrm{s_j^X}\right)^2}\right)\mathrm{du} \tag{8}$$

where $\log\widehat{L}(\theta)$ denotes the value of the maximized loglikelihood objective function, n is the number of components, and N is the number of data points, X_i is the i^{th} mechanical data, μ is the statistic mean, and s is the covariance matrix, which is a square matrix giving the covariance between each pair of elements of a given vector.

BIC analyses are performed 500 times for each preset component number n (from 2 to 10) and each type of covariance matrix (diagonal or full; shared or unshared) to avoid a random error. The covariance matrix determines the shape of the confidence ellipsoid drawn over each cluster. In this study, we investigated whether the covariance matrices are diagonal or full, and whether all components have the same covariance matrix (shared or unshared). Fig. 15a and b summarize the BIC analysis for quartz and illite phases, respectively, indicating that a two-component mixture (n = 2) with a full-unshared covariance matrix provides the best representation. The modulus and hardness of these intact particles and nano-porous aggregates are then extracted by GMM clustering, as shown in Fig. 15c and d. The shaded ellipsoids are generated based on the statistical confidence level of 95% and the covariance matrix, which determines the length of the major and minor axes, and the orientation of the axes, respectively.

To further address the effect of particle size on the mechanical properties, the measured Young's modulus and hardness of a pure mineral phase were linked to the particle sizes obtained from the edge detection algorithm. In all five pure mineral phases in the Longmaxi shale (i.e., excluding organics), Young's modulus and hardness initially increased with the particle area and then were relatively constant after the particle area exceeded a specific threshold value. Young's modulus and hardness of intact mineral particles were thus obtained (Table 2). Compared to the results from the coupled analysis only (Fig. 12), with these considerations of particle size effects, the mechanical properties of the constituent phases were further refined and show a better agreement with the values for the same mineral phases reported in the literature, as shown in Table 2.

4. Discussion

Shales are composite materials with high heterogeneity and complex multi-phase characteristics. Fig. 16 presents a conceptual 5-level (multi-scale) representation of shale extending from the nano-scale clay unit to the centimeter-scale macroscopic shale.

Level 0 corresponds to the elementary unit of clay minerals at the nanometer scale (0.7 nm and 1.0 nm in thickness for the 1:1 and 2:1 phyllosilicate clay minerals, respectively (Zhang et al., 2010)). Level I corresponds to the aggregated clay, which typically comprises assemblies of particles in face-face configurations: illite aggregates generally are up to 10 nm thick with surface dimensions ~500–1500 nm (Nadeau, 1985). Level II is the scale of the ductile porous clay/organic aggregate

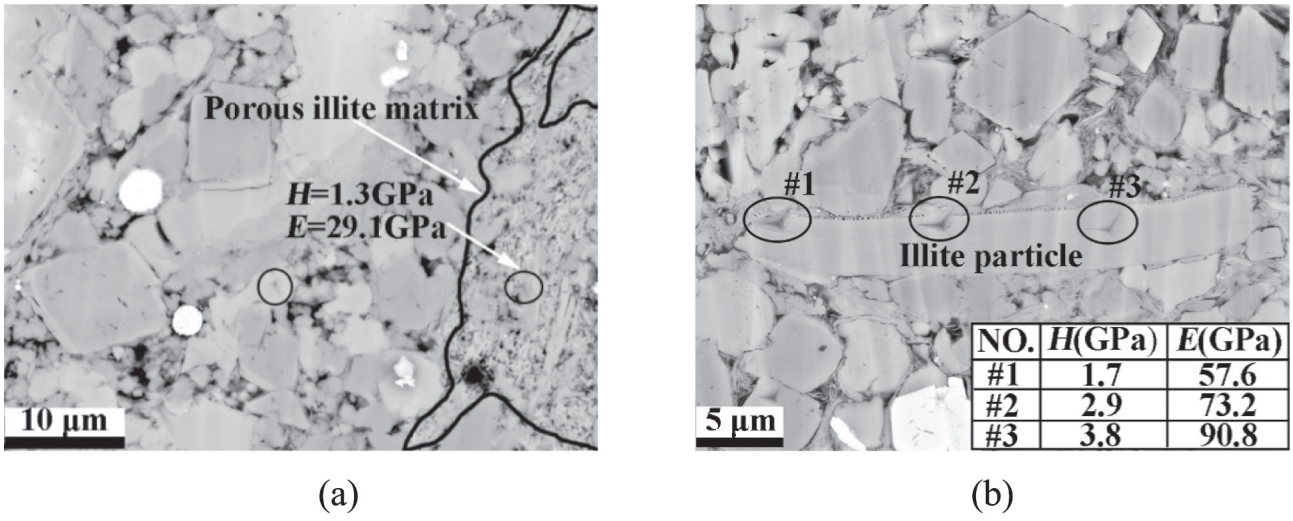

NO.	H(GPa)	E(GPa)
#1	1.7	57.6
#2	2.9	73.2
#3	3.8	90.8

Fig. 14. BSE images of illite phase in Longmaxi shale samples. a) Nano-porous illite matrix with much lower hardness and Young's modulus than b) Intact illite particle. The residual indentation footprints are circled in the images.

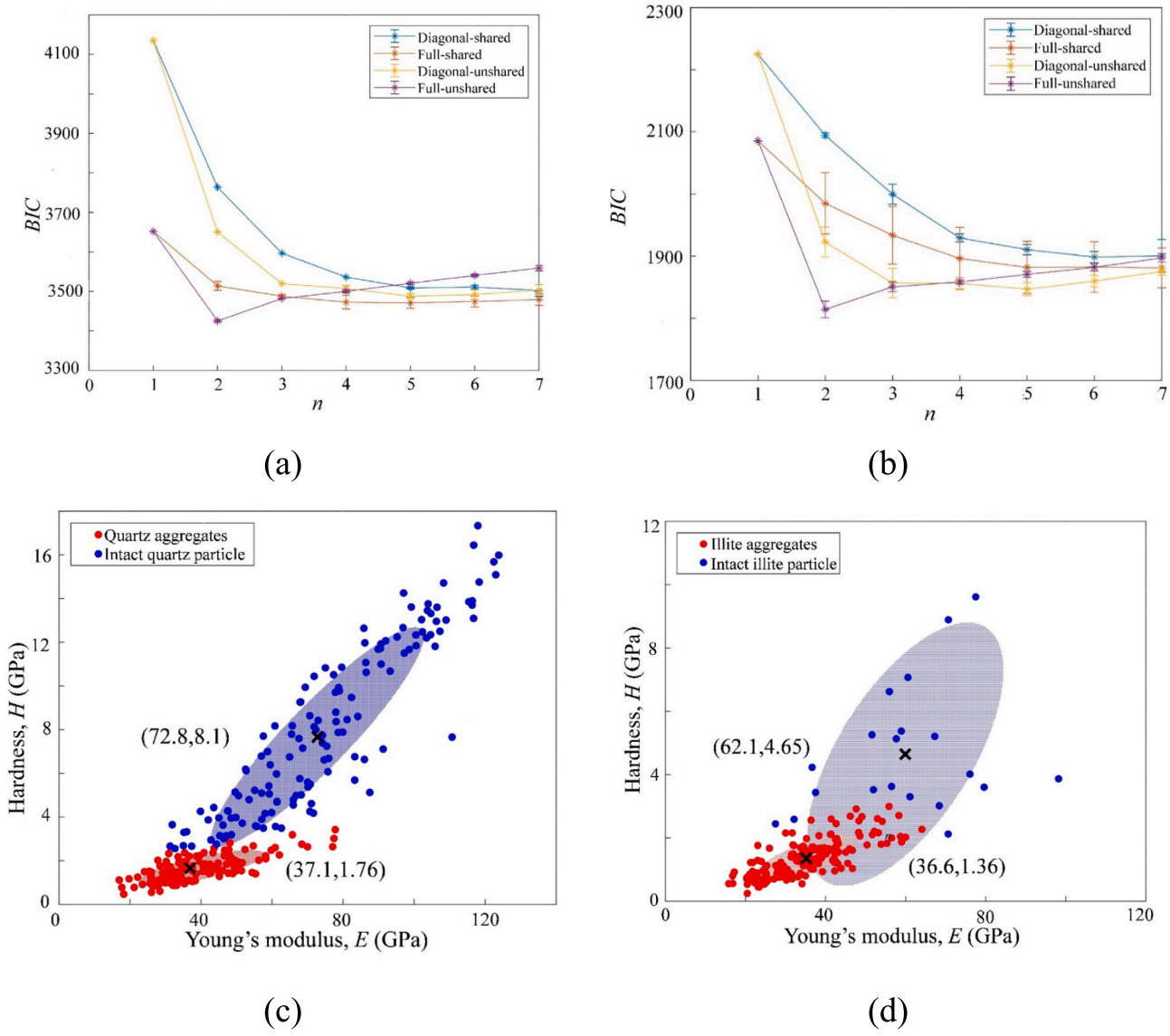

Fig. 15. Refined mechanical properties obtained by BIC and GMM analysis for quartz and illite. a) and b) Optimal components ($n = 2$) based on BIC analysis for quartz and illite, respectively; c) and d) GMM analyses used to establish statistical mean values of Young's modulus and hardness for the intact and nano-porous aggregate components of quartz and illite, respectively.

and the brittle mineral particles. Level III corresponds to the representative unit of the macroscopic shale at the submillimeter scale, including both the ductile and brittle minerals. Thus, this scale is considered as the elementary building block of shale. Level IV is the scale of macroscopic shale, which is the object of conventional, macroscopically-homogeneous laboratory studies. Precise prediction and characterization of the multi-scale mechanical properties of shale are of great scientific importance and engineering significance.

Upscaling of Level II to III has been widely carried out in prior studies using self-consistent and Mori-Tanaka approaches (Liu et al., 2018; Liu et al., 2022; Luo et al., 2021). In this study, a multi-scale model for upscaling mineral particles (Level I) to their nano-porous aggregates (Level II) was analyzed for the first time based on a self-consistent scheme for granular morphology, accounting for the nanoscale porosity of shale materials (Seiphoori et al., 2017). Young's moduli of Longmaxi shale samples at Levels I and II are obtained by the coupled analysis described in this study. These experimental data can provide both the input parameters and the experimental validation for the multi-scale mechanical model.

In the case of linear, isotropic, and elastic behavior of the mineral phases, a self-consistent model (Dormieux et al., 2006; Zaoui, 2002) was established for homogenizing the stiffness of a mixture with granular morphology:

$$\mathrm{K_{hom}} = \sum_i \varphi_i \mathrm{K_i}\left(1+\alpha_0\left(\frac{\mathrm{K_i}}{\mathrm{K_{hom}}}-1\right)\right)^{-1}\left[\sum_i \varphi_i\left(1+\alpha_0\left(\frac{\mathrm{K_i}}{\mathrm{K_{hom}}}-1\right)\right)^{-1}\right]^{-1} \tag{9}$$

$$\mathrm{G_{hom}} = \sum_i \varphi_i \mathrm{G_i}\left(1+\beta_0\left(\frac{\mathrm{G_i}}{\mathrm{G_{hom}}}-1\right)\right)^{-1}\left[\sum_i \varphi_i\left(1+\beta_0\left(\frac{\mathrm{G_i}}{\mathrm{G_{hom}}}-1\right)\right)^{-1}\right]^{-1} \tag{10}$$

where K_{hom} and G_{hom} are the homogenized bulk modulus and shear modulus, respectively; K_i, G_i and φ_i are the bulk modulus, shear modulus, and volume fraction of the i-th phase, respectively. Finally, α_0 and β_0 are defined by $\alpha_0 = \frac{3K_{\mathrm{hom}}}{3K_{\mathrm{hom}}+4G_{\mathrm{hom}}}$, and $\beta_0 = \frac{6(K_{\mathrm{hom}}+2G_{\mathrm{hom}})}{5(3K_{\mathrm{hom}}+4G_{\mathrm{hom}})}$.

The upscaling of strength properties requires the use of non-linear

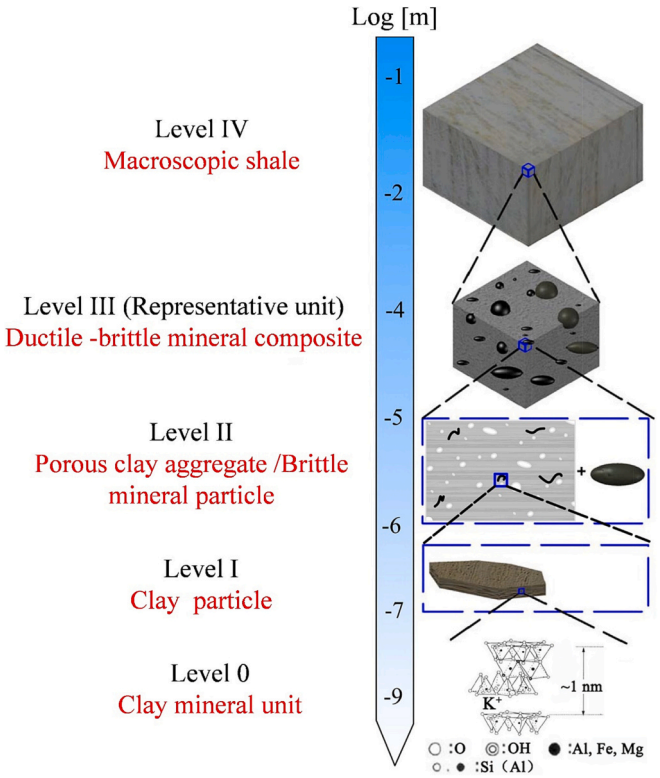

Fig. 16. Multi-scale model of shale structure.

homogenization theory (Bobko et al., 2011):

$$H_{\text{hom}} = h_s \times \Pi_H(\eta, \mu) \tag{11}$$

where Π_H is a dimensionless function to be developed, H_{hom} and h_s are the homogenized hardness and the particle hardness, respectively, and η and μ are the solid packing density and friction coefficient, respectively. Based on data analysis, Gathier (2008) obtained the scaling relations between the particle hardness, h_s, and the homogenized hardness, H_{hom}, for a porous composite exhibiting self-consistent morphology (after Bobko et al. (2011)):

$$\Pi_H(\eta, \mu) = \Pi_1(\eta) + \mu(1-\eta)\Pi_2(\eta, \mu) \tag{12}$$

$$\Pi_1(\eta) = \frac{\sqrt{2(2\eta-1)} - (2\eta-1)}{\sqrt{2}-1}\left[1 - 5.3678(1-\eta) + 12.1933(1-\eta)^2 - 10.3071(1-\eta)^3\right] \tag{13}$$

$$\Pi_{II}(\eta, \mu) = \frac{2\eta-1}{2}\left[6.7374 - 39.5893(1-\eta) + 34.3216(1-\eta)\mu - 21.2053\mu^3\right] \tag{14}$$

The quartz and illite phases of Longmaxi shale include intact particles and nano-porous aggregates (level II; Fig. 15) that can be considered as a granular material and upscaled using self-consistent assumptions. Young's modulus and hardness of the intact particles are determined by the GMM fitting of the grid nanoindentation data. However, the packing density/porosity of the nano-porous aggregates (η = 1-φ) is not measured directly in this study.

Fig. 17a shows the relationships of the homogenized stiffness [Eqs. (9), and (10)] as a function of the stiffness of intact particles (i.e., at φ = 0) and the porosity of the nano-aggregates for illite and quartz phases.

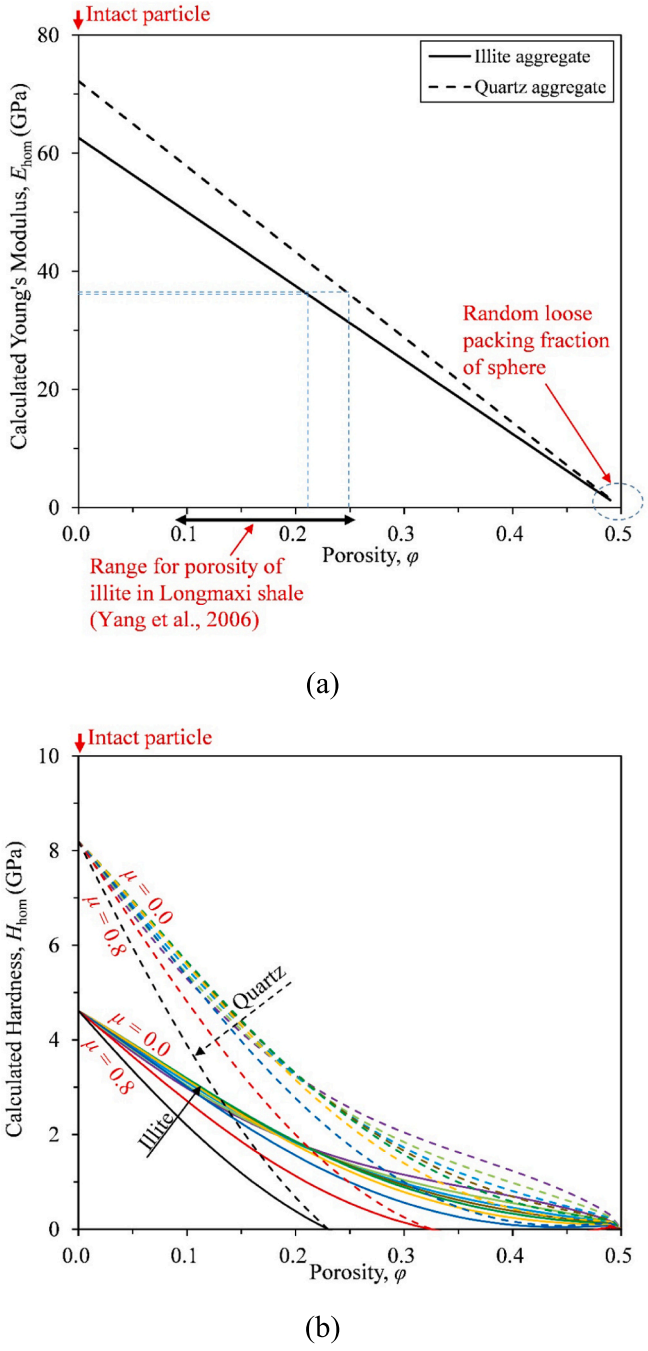

Fig. 17. Self-consistent homogenized a) Young's modulus, E; and b) hardness, H, for nano-porous quartz and illite aggregates as functions of assumed nano-porosity, φ. H values are shown at selected friction ratios, μ = 0.0–0.8 (0.1 interval).

These results show that the self-consistent formulation explains the difference in mean values of E for intact and nano-porous aggregates with φ = 0.21, 0.25 for illite and quartz, respectively. The estimate of nano-porosity for illite is also within the range reported from nitrogen adsorption measurements on Longmaxi shale by Yang et al. (2016). The increased porosity results in lower homogenized stiffness and hardness for both the illite and quartz aggregates. As the porosity equals zero, the composite material becomes an intact particle. Thus, the calculated

stiffness and hardness [E, H] reflect the properties of the intact illite and quartz particles, i.e., [62.1 GPa/4.65 GPa] and [72.8 GPa/8.10 GPa], respectively.

Fig. 17b shows the homogenized hardness for the nano-porous quartz and illite aggregates [based on Eqs. (9)–(11)] as functions of intact particle hardness, nano-porosity, and selected values of the friction coefficient μ. There have been extensive studies of the inter-particle friction for quartz (e.g., summarized in Terzaghi et al. (1996), suggesting an average value $\mu = 0.4$, and thus an estimated homogenized hardness, $H = 2.4$ GPa. This value is higher than the mean (1.8 GPa) reported in Fig. 15a but is within the range measured for nano-porous quartz in Longmaxi shale. Similarly, the interparticle friction of illite has been reported in the range $\mu = 0.40 \pm 0.04$, corresponding to a homogenized hardness, $H = (1.7 \pm 0.02)$ GPa from the self-consistent analyses (Fig. 17b), which is within the range identified by GMM analyses of nano-porous illite (Fig. 15b).

5. Conclusions

In this study, we developed a coupled analysis of grid nanoindentation and in-situ mineralogical identification considering the particle size effect to access the mechanical properties of the constituent mineral phases. Furthermore, multi-scale mechanical models for upscaling the elastic stiffness and strength properties were established, with considerations of the self-consistent scheme for granular morphology to link the microscopic characteristics with the multi-scale mechanical properties of shales. The key conclusions of this study are as follows:

1. By combining digital images of mineral distribution and control coordinates for grid nanoindentation, Mechanical properties (hardness and Young's modulus) for five pure mineral phases (i.e., calcite, dolomite, quartz, pyrite, and illite) and three mineral mixture phases (i.e., brittle, ductile, and composite mixtures) are extracted for specimens of carbonate-rich Longmaxi shale.
2. Threshold particle sizes were identified for estimating intact mineral properties based on a probabilistic interpretation of the indentation footprint. The identified characteristic length for extracting the mechanical properties of constituent mineral phases from the grid nanoindentation technique is about 5.8–11.7 μm, i.e., up to 10 times greater than that proposed in prior research.
3. The mechanical properties of shale mineral phases are influenced by particle size and morphology, particularly for quartz and illite phases. These phases are further partitioned (through statistical BIC and two-dimensional GMM analyses) to distinguish between the mechanical properties of individual particles and nano-porous aggregates.
4. A multi-scale model for upscaling from mineral particles (Level I) to their nano-porous aggregates (Level II) is analyzed for the first time based on a self-consistent scheme for granular morphology. The self-consistent modeling approach can explain the measured differences in elastic stiffness and hardness properties of the mineral aggregates and their intact particles. This provides a clear basis for upscaling properties from the microscopic characteristics (i.e., the volume fractions and the mechanical properties of the intact mineral particles) measured by the proposed coupling analysis.

CRediT authorship contribution statement

Jianting Du: Investigation, Methodology, Writing – original draft, Conceptualization, Writing – review & editing. **Andrew J. Whittle:** Conceptualization, Funding acquisition, Methodology, Project administration, Supervision, Writing – review & editing. **Liming Hu:** Funding acquisition, Supervision, Writing – review & editing. **Thibaut Divoux:** Investigation, Writing – review & editing, Methodology. **Jay N. Meegoda:** Funding acquisition, Supervision, Writing – review & editing.

Declaration of Competing Interest

The authors declare that they have no known competing financial interests or personal relationships that could have appeared to influence the work reported in this paper.

Data availability

Data will be made available on request.

Acknowledgments

This research was funded by the National Natural Science Foundation of China (Project No. 51979144, 51661165015, and 51323014) and the Open Research Fund Program of State Key Laboratory of Hydroscience and Engineering (Project Number: sklhse-2023-D-04). The authors gratefully acknowledge the support of the Concrete Sustainability Hub in the MIT Department of Civil and Environmental Engineering for access to facilities and assistance in conducting this research.

Appendix A. Surface preparation

Argon Milling

The trimmed shale samples are polished with the coarse abrasive paper into 1 cm × 1 cm × 0.5 cm thick blocks as required by the JEOL cross-section polisher. The maximum accelerating voltage of 6 kV is applied to minimize the heat damage, and the milling duration is set to 10–12 h. Typically, 50–100 μm deep materials are removed from the surface to ensure that the milled surface is free of mechanical polishing artifacts as well as smearing due to razor blade cutting.

AFM roughness characterization of shale samples prepared by mechanical polishing and Argon milling (Fig. A1) show RMS roughness, $R_q = 15$ nm and 50 nm, respectively. Trenching is a common, unwanted side effect of ion beam milling (Youngner and Haynes, 1982), that can result in an increase in the roughness of a milled surface.

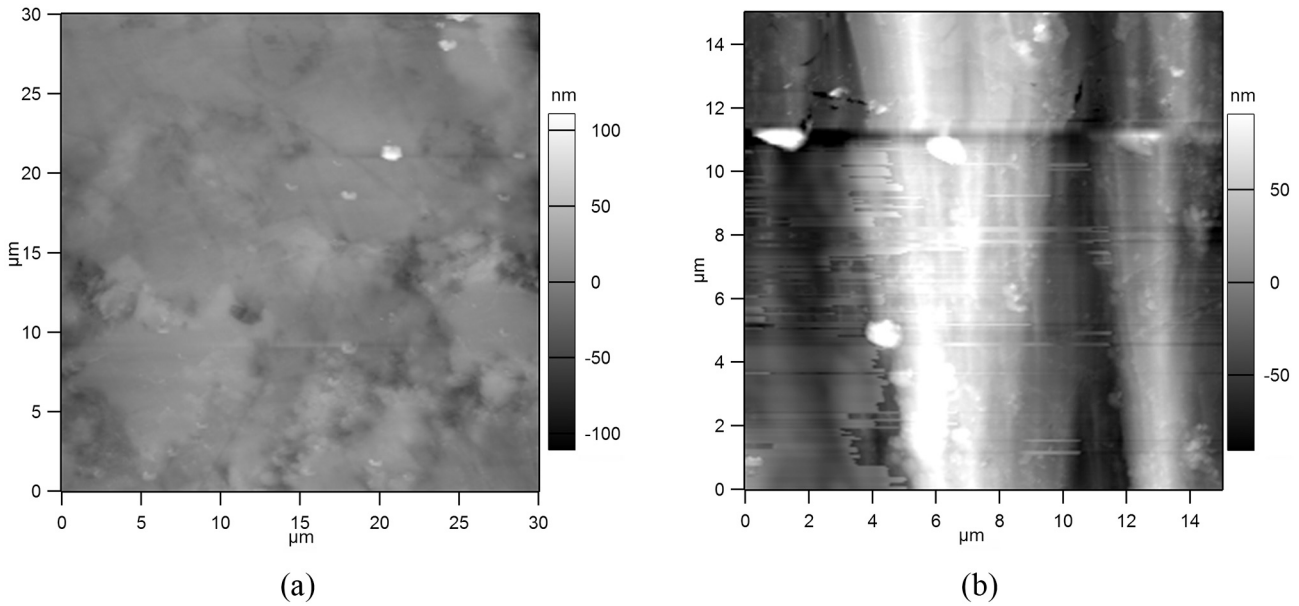

Fig. A1. Representative AFM maps of interested regions prepared by mechanical polishing (a) and Argon milling (b). The dimensions of AFM images are 30 μm by 30 μm and 15 μm by 15 μm, respectively, and the measured surface roughness, R_q = 16 nm and R_q = 50 nm, respectively.

The surface roughness effect on nanoindentation testing from mechanical polishing and Argon milling is analyzed contrastively. As shown in Fig. A2, the Young modulus and hardness data of the mechanical-polishing sample and Argon-milling sample are in good accordance with each other, i.e., these two surface preparation create qualified surface conditions for nanoindentation testing. Due to its ease of use and high efficiency, mechanical polishing is employed for the surface preparation in this study.

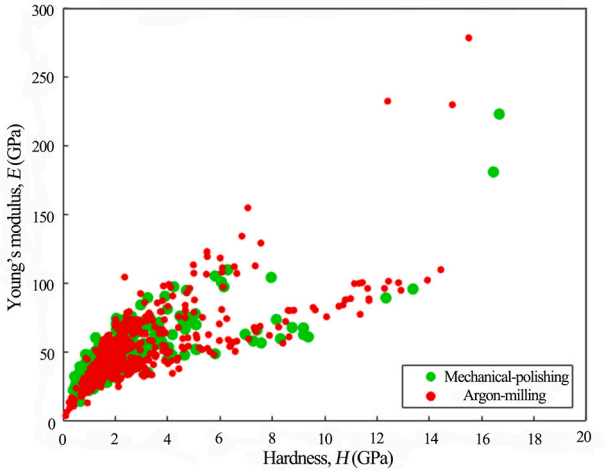

Fig. A2. Comparison of Young's modulus and hardness data between the mechanical-polishing sample (green points) and Argon-milling sample (red points). (For interpretation of the references to colour in this figure legend, the reader is referred to the web version of this article.)

References

Abedi, S., Slim, M., Hofmann, R., Bryndzia, T., Ulm, F., 2016. Nanochemo-mechanical signature of organic-rich shales: a coupled indentation–EDX analysis. Acta Geotech. 11, 559–572. https://doi.org/10.1007/s11440-015-0426-4.

Aguilar-Santillan, J., 2008. Elastic and hardness anisotropy and the indentation size effect of pyrite (FeS2) single crystal. Acta Mater. 56, 2476–2487. https://doi.org/10.1016/j.actamat.2008.01.022.

Allen, M., Poggiali, D., Whitaker, K.J., Marshall, T.R., Kievit, R.A., 2019. Raincloud plots: a multi-platform tool for robust data visualization. Wellcome Open Res. 4, 63.

Bobji, M.S., Biswas, S.K., 1999. Deconvolution of hardness from data obtained from nanoindentation of rough surfaces. J. Mater. Res. 14, 2259–2268. https://doi.org/10.1557/JMR.1999.0302.

Bobko, C.P., Ulm, F., 2008. The nano-mechanical morphology of shale. Mech. Mater. 40, 318–337. https://doi.org/10.1016/j.mechmat.2007.09.006.

Bobko, C.P., Gathier, B., Ortega, J.A., Ulm, F., Borges, L., Abousleiman, Y.N., 2011. The nanogranular origin of friction and cohesion in shale—a strength homogenization approach to interpretation of nanoindentation results. Int. J. Numer. Anal. Methods Geomech. 35, 1854–1876. https://doi.org/10.1002/nag.984.

Boosari, S.S.H., Aybar, U., Eshkalak, M.O., 2015. Carbon dioxide storage and sequestration in unconventional shale reservoirs. J. Geosci. Environ. Protect. 03, 7–15. https://doi.org/10.4236/gep.2015.31002.

Broz, M.E., Cook, R.F., Whitney, D.L., 2006. Microhardness, toughness, and modulus of Mohs scale minerals. Am. Mineral. 91, 135–142. https://doi.org/10.2138/am.2006.1844.

Chen, P., Han, Q., Ma, T., Lin, D., 2015. The mechanical properties of shale based on micro-indentation test. Pet. Explor. Dev. 42, 723–732. https://doi.org/10.1016/S1876-3804(15)30069-0.

Chen, J., Lan, H., Macciotta, R., Wu, Y., Li, Q., Zhao, X., 2018. Anisotropy rather than transverse isotropy in Longmaxi shale and the potential role of tectonic stress. Eng. Geol. 247, 38–47. https://doi.org/10.1016/j.enggeo.2018.10.018.

Constantinides, G., Chandran, K.S.R., Ulm, F., Van Vliet, K.J., 2006. Grid indentation analysis of composite microstructure and mechanics: principles and validation. Mater. Sci. Eng. A-struct. Mater. Prop. Microstruct. Process. 430, 189–202. https://doi.org/10.1016/j.msea.2006.05.125.

Dai, J., Zou, C., Liao, S., Dong, D., Ni, Y., Huang, J., Wu, W., Gong, D., Huang, S., Hu, G., 2014. Geochemistry of the extremely high thermal maturity Longmaxi shale gas, southern Sichuan Basin. Org. Geochem. 74, 3–12. https://doi.org/10.1016/j.orggeochem.2014.01.018.

Deirieh, A., Ortega, J.A., Ulm, F., Abousleiman, Y.N., 2012. Nanochemomechanical assessment of shale: a coupled WDS-indentation analysis. Acta Geotech. 7, 271–295. https://doi.org/10.1007/s11440-012-0185-4.

Dong, T., He, S., Chen, M., Hou, Y., Guo, X., Wei, C., Han, Y., Yang, R., 2019. Quartz types and origins in the paleozoic Wufeng-Longmaxi Formations, Eastern Sichuan Basin, China: implications for porosity preservation in shale reservoirs. Mar. Pet. Geol. 106, 62–73. https://doi.org/10.1016/j.marpetgeo.2019.05.002.

Donnelly, E., Baker, S.P., Boskey, A.L., Der Meulen, M.C.H.V., 2006. Effects of surface roughness and maximum load on the mechanical properties of cancellous bone measured by nanoindentation. J. Biomed. Mater. Res. Part A 77, 426–435. https://doi.org/10.1002/jbm.a.30633.

Dormieux, L., Kondo, D., Ulm, F.-J., 2006. Microporomechanics. John Wiley & Sons.

Du, J., Hu, L., Meegoda, J.N., Zhang, G., 2018. Shale softening: observations, phenomenological behavior, and mechanisms. Appl. Clay Sci. 161, 290–300. https://doi.org/10.1016/j.clay.2018.04.033.

Du, J., Whittle, A.J., Hu, L., Divoux, T., Meegoda, J.N., 2021. Characterization of meso-scale mechanical properties of Longmaxi shale using grid microindentation experiments. J. Rock Mech. Geotech. Eng. 13, 555–567. https://doi.org/10.1016/j.jrmge.2020.09.009.

Durst, K., Backes, B., Göken, M., 2005. Indentation size effect in metallic materials: correcting for the size of the plastic zone. Scr. Mater. 52, 1093–1097. https://doi.org/10.1016/j.scriptamat.2005.02.009.

Eliyahu, M., Emmanuel, S., Daystirrat, R.J., Macaulay, C.I., 2015. Mechanical properties of organic matter in shales mapped at the nanometer scale. Mar. Pet. Geol. 59, 294–304. https://doi.org/10.1016/j.marpetgeo.2014.09.007.

Elliot, T.R., Celia, M.A., 2012. Potential restrictions for CO2 sequestration sites due to shale and tight gas production. Environ. Sci. Technol. 46, 4223–4227. https://doi.org/10.1021/es2040015.

Gathier, B., 2008. Multiscale Strength Homogenization: Application to Shale Nanoindentation. Massachusetts Institute of Technology.

Guo, Z., Li, X.-Y., Liu, C., Feng, X., Shen, Y., 2013. A shale rock physics model for analysis of brittleness index, mineralogy and porosity in the Barnett Shale. J. Geophys. Eng. 10, 025006 https://doi.org/10.1088/1742-2132/10/2/025006.

Jiu, B., Huang, W., He, M., Lv, C., Liang, F., 2018. Quantitative analysis of micron-scale and nano-scale pore throat characteristics of tight sandstone using matlab. Appl. Sci. 8, 1272. https://doi.org/10.3390/app8081272.

Jiu, B., Huang, W., Li, Y., 2020. An approach for quantitative analysis of cementation in sandstone based on cathodoluminescence and MATLAB algorithms. J. Pet. Sci. Eng. 186, 106724 https://doi.org/10.1016/j.petrol.2019.106724.

Kuila, U., McCarty, D.K., Derkowski, A., Fischer, T.B., Topór, T., Prasad, M., 2014. Nano-scale texture and porosity of organic matter and clay minerals in organic-rich mudrocks. Fuel 135, 359–373. https://doi.org/10.1016/j.fuel.2014.06.036.

Kumar, V., Sondergeld, C.H., Rai, C.S., 2012. Nano to macro mechanical characterization of shale. In: SPE Annual Technical Conference and Exhibition. Society of Petroleum Engineers, San Antonio, Texas, USA.

Li, C., Ostadhassan, M., Gentzis, T., Kong, L., Carvajalortiz, H., Bubach, B., 2018. Nanomechanical characterization of organic matter in the Bakken formation by microscopy-based method. Mar. Pet. Geol. 96, 128–138. https://doi.org/10.1016/j.marpetgeo.2018.05.019.

Li, L., Huang, B., Tan, Y., Li, X., Ranjith, P., 2022. Using micro-indentation to determine the elastic modulus of shale laminae and its implication: cross-scale correlation of elastic modulus of mineral and rock. Mar. Pet. Geol. 143, 105740 https://doi.org/10.1016/j.marpetgeo.2022.105740.

Liu, K., Ostadhassan, M., Bubach, B., Ling, K., Tokhmechi, B., Robert, D., 2018. Statistical grid nanoindentation analysis to estimate macro-mechanical properties of the Bakken Shale. J. Nat. Gas Sci. Eng. 53, 181–190. https://doi.org/10.1016/j.jngse.2018.03.005.

Liu, Y., Liu, S., Kang, Y., 2021. Probing nanomechanical properties of a shale with nanoindentation: heterogeneity and the effect of water–shale interactions. Energy Fuel 35, 11930–11946. https://doi.org/10.1021/acs.energyfuels.1c01328.

Liu, Y., Liu, A., Liu, S., Kang, Y., 2022. Nano-scale mechanical properties of constituent minerals in shales investigated by combined nanoindentation statistical analyses and SEM-EDS-XRD techniques. Int. J. Rock Mech. Min. Sci. 159, 105187 https://doi.org/10.1016/j.ijrmms.2022.105187.

Loberg, B.E., Háber, M., Westberg, S.-B., 1985. Microhardness, reflectance and unit cell length of pyrites from Swedish base metal ores. Geologiska Föreningen i Stockholm Förhandlingar 107, 45–52. https://doi.org/10.1080/11035898509452612.

Luo, S., Lu, Y., Wu, Y., Song, J., DeGroot, D.J., Jin, Y., Zhang, G., 2020. Cross-scale characterization of the elasticity of shales: statistical nanoindentation and data analytics. J. Mech. Phys. Solids 140, 103945. https://doi.org/10.1016/j.jmps.2020.103945.

Luo, S., Kim, D., Wu, Y., Li, Y., Wang, D., Song, J., DeGroot, D.J., Zhang, G., 2021. Big data nanoindentation and analytics reveal the multi-staged, progressively-homogenized, depth-dependent upscaling of rocks' properties. Rock Mech. Rock. Eng. 54, 1501–1532. https://doi.org/10.1007/s00603-020-02337-3.

Mashhadian, M., Verde, A., Sharma, P., Abedi, S., 2018. Assessing mechanical properties of organic matter in shales: results from coupled nanoindentation/SEM-EDX and micromechanical modeling. J. Pet. Sci. Eng. 165, 313–324.

Middleton, R.S., Viswanathan, H.S., Currier, R.P., Gupta, R., 2014. CO2 as a fracturing fluid: potential for commercial-scale shale gas production and CO2 sequestration. Energy Procedia 63, 7780–7784. https://doi.org/10.1016/j.egypro.2014.11.812.

Nadeau, P., 1985. The physical dimensions of fundamental clay particles. Clay Miner. 20, 499–514. https://doi.org/10.1180/claymin.1985.020.4.06.

Neuzil, C.E., 2013. Can shale safely host U.S. nuclear waste. EOS Trans. Am. Geophys. Union 94, 261–262. https://doi.org/10.1002/2013EO300001.

Oliver, W.C., Pharr, G.M., 1992. An improved technique for determining hardness and elastic modulus using load and displacement sensing indentation experiments. J. Mater. Res. 7, 1564. https://doi.org/10.1557/JMR.1992.1564.

Oliver, WC, Pharr, GM., 2004. Measurement of hardness and elastic modulus by instrumented indentation: Advances in understanding and refinements to methodology. J Mater 19, 3–20. https://doi.org/10.1557/jmr.2004.19.1.3.

Seiphoori, A., Whittle, A.J., Krakowiak, K.J., Einstein, H.H., 2017. Insights into diagenesis and pore structure of opalinus shale through comparative studies of natural and reconstituted materials. Clay Clay Miner. 65, 135–153. https://doi.org/10.1346/CCMN.2017.064055.

Shukla, P., Kumar, V., Curtis, M., Sondergeld, C.H., Rai, C.S., 2013. Nanoindentation studies on shales. In: 47th US Rock Mechanics/Geomechanics Symposium. American Rock Mechanics Association, San Francisco, California, USA.

Simpson, G.J., Sedin, D.L., Rowlen, K.L., 1999. Surface roughness by contact versus tapping mode atomic force microscopy. Langmuir 15, 1429–1434. https://doi.org/10.1021/la981024a.

Terzaghi, K., Peck, R.B., Mesri, G., 1996. Soil Mechanics in Engineering Practice, 3rd Edition. John Wiley and Sons, Inc, New York.

Ulm, F., Abousleiman, Y.N., 2006. The nanogranular nature of shale. Acta Geotech. 1, 77–88. https://doi.org/10.1007/s11440-006-0009-5.

Ulm, F., Vandamme, M., Bobko, C.P., Ortega, J.A., Tai, K., Ortiz, C., 2007. Statistical indentation techniques for hydrated nanocomposites: concrete, bone, and shale. J. Am. Ceram. Soc. 90, 2677–2692. https://doi.org/10.1111/j.1551-2916.2007.02012.x.

Veytskin, Y., Tammina, V.K., Bobko, C.P., Hartley, P.G., Clennell, M.B., Dewhurst, D.N., Dagastine, R.R., 2017. Micromechanical characterization of shales through nanoindentation and energy dispersive x-ray spectrometry. Geomech. Energy Environ. 9, 21–35.

Viktorov, S., Golovin, Y.I., Kochanov, A., Tyurin, A., Shuklinov, A., Shuvarin, I., Pirozhkova, T., 2014. Micro-and nano-indentation approach to strength and deformation characteristics of minerals. J. Min. Sci. 50, 652–659. https://doi.org/10.1134/S1062739114040048.

Woodcock, C., Bahr, D., 2000. Plastic zone evolution around small scale indentations. Scr. Mater. 43, 783–788. https://doi.org/10.1016/S1359-6462(00)00489-9.

Wu, L.C., Yu, C., 2012. Powder particle size measurement with digital image processing using Matlab. Adv. Mater. Res. Trans. Tech. Publ. 589–593.

Wu, Y., Li, Y., Luo, S., Lu, M., Zhou, N., Wang, D., Zhang, G., 2020. Multiscale elastic anisotropy of a shale characterized by cross-scale big data nanoindentation. Int. J. Rock Mech. Min. Sci. 134, 104458 https://doi.org/10.1016/j.ijrmms.2020.104458.

Xian, S., Jiang, S., Shuangfang, L., Zhiliang, H., Dongjie, L., Zhixuan, W., Dianshi, X., 2019. Investigation of mechanical properties of bedded shale by nanoindentation tests: a case study on Lower Silurian Longmaxi Formation of Youyang area in Southeast Chongqing, China. Pet. Explor. Dev. 46, 163–172. https://doi.org/10.1016/S1876-3804(19)30016-3.

Xu, J., Tang, X., Wang, Z., Feng, Y., Bian, K., 2020. Investigating the softening of weak interlayers during landslides using nanoindentation experiments and simulations. Eng. Geol. 277, 105801 https://doi.org/10.1016/j.enggeo.2020.105801.

Xu, H., Zhou, W., Hu, Q., Yi, T., Ke, J., Zhao, A., Lei, Z., Yu, Y., 2021. Quartz types, silica sources and their implications for porosity evolution and rock mechanics in the Paleozoic Longmaxi Formation shale, Sichuan Basin. Mar. Pet. Geol. 128, 105036 https://doi.org/10.1016/j.marpetgeo.2021.105036.

Yang, R., He, S., Yi, J., Hu, Q., 2016. Nano-scale pore structure and fractal dimension of organic-rich Wufeng-Longmaxi shale from Jiaoshiba area, Sichuan Basin: investigations using FE-SEM, gas adsorption and helium pycnometry. Mar. Pet. Geol. 70, 27–45. https://doi.org/10.1016/j.marpetgeo.2015.11.019.

Youngner, D., Haynes, C., 1982. Modeling ion beam milling. J. Vac. Sci. Technol. 21, 677–680. https://doi.org/10.1116/1.571812.

Zaoui, A., 2002. Continuum micromechanics: survey. J. Eng. Mech-Asce 128, 808–816. https://doi.org/10.1061/(ASCE)0733-9399(2002)128:8(808).

Zhang, G., Wei, Z., Ferrell, R.E., 2009. Elastic modulus and hardness of muscovite and rectorite determined by nanoindentation. Appl. Clay Sci. 43, 271–281. https://doi.org/10.1016/j.clay.2008.08.010.

Zhang, G., Wei, Z., Ferrell, R.E., Guggenheim, S., Cygan, R.T., Luo, J., 2010. Evaluation of the elasticity normal to the basal plane of non-expandable 2:1 phyllosilicate minerals by nanoindentation. Am. Mineral. 95, 863–869. https://doi.org/10.2138/am.2010.3398.

Zhou, B., Wang, J., Wang, H., 2018. Three-dimensional sphericity, roundness and fractal dimension of sand particles. Géotechnique 68, 18–30. https://doi.org/10.1680/jgeot.16.P.207.